

Evolutionary tracks of massive stars during formation

Michael D. Smith ¹*

¹*Centre for Astrophysics & Planetary Science, University of Kent, Canterbury CT2 7NH, UK*

Accepted Received ; in original form

ABSTRACT

A model for massive stars is constructed by piecing together evolutionary algorithms for the protostellar structure, the environment, the inflow and the radiation feedback. We investigate specified accretion histories of constant, decelerating and accelerating forms and consider both hot and cold accretion, identified with spherical free-fall and disk accretion, respectively. Diagnostic tools for the interpretation of the phases of massive star formation and testing the evolutionary models are then developed. Evolutionary tracks able to fit Herschel Space Telescope data require the generated stars to be three to four times less massive than in previous interpretations, thus being consistent with clump star formation efficiencies of 10 – 15%. However, for these cold Herschel clumps, the bolometric temperature is not a good diagnostic to differentiate between accretion models. We also find that neither spherical nor disk accretion can explain the high radio luminosities of many protostars. Nevertheless, we discover a solution in which the extreme ultraviolet flux needed to explain the radio emission is produced if the accretion flow is via free-fall on to hot spots covering less than 10% of the surface area. Moreover, the protostar must be compact, and so has formed through cold accretion. We show that these conclusions are independent of the imposed accretion history. This suggests that massive stars form via gas accretion through disks which, in the phase before the star bloats, download their mass via magnetic flux tubes on to the protostar.

Key words: stars: formation, stars: protostars, stars: pre-main-sequence, ISM: jets and outflows

1 INTRODUCTION

Massive stars are the principal source of heavy elements and ultraviolet radiation, and a major supplier of wind and supernova energy, within the Universe. Individually, they dominate cluster formation and, collectively, they influence the evolution of galaxies. However, our knowledge of massive stars remains limited (Zinnecker & Yorke 2007). We know they are born in massive and dense clumps embedded within giant molecular clouds (Blitz 1991). We also think we understand fairly well how physical mechanisms conspire to describe the emergence of low- and intermediate-mass stars. But the events which conspire to produce the high-mass counterparts are still controversial (McKee & Ostriker 2007). This is due to a combination of factors including their rarity, large distances, rapid evolution, high extinction and their confusion with associated clusters.

A formation model requires integration of evolutionary models for the internal star, the environment and the feedback. Together, these constitute a ‘protostellar system’

which consists of several distinct components including a hydrostatic core, disk, envelope, wind, jets and bipolar outflow. Recently, with Herschel, BLAST and Planck following Spitzer (e.g. Elia et al. 2010; Netterfield et al. 2009; Planck Collaboration et al. 2011), we have acquired the quality and quantity of data to explore the early formation stages. Processes that can now be addressed include clump dispersal, cluster formation, mass inflow, stellar accretion, stellar flux and mass outflow.

The aim here is to link the system components and underlying processes together through a model framework that predicts resulting observable correlations. We thus develop a scheme which explores plausible paths from clump to exposed star. It is set up to track how mass is passed between the components, while accounting for direct ejection from the supplying clump and indirect ejection through jets.

The interaction of a gradually emerging star with a massive clump is described in terms of a time sequence going from compact and hot molecular cores to extended H II regions (Churchwell 2002) as expansion occurs. This has emphasized an issue concerning the time scales with too many bound hypercompact or the later ultracompact H II

* E-mail: m.d.smith@kent.ac.uk

regions being observed. This may be resolved by taking less ideal approaches to accretion and dispersal from and to the clump (Peters et al. 2010), allowing for choking of the cavity through the infall of dense filaments and fragments of the clump.

The very early stages of protostar formation within cold clumps have now been identified in large numbers as Infrared Dark Clouds (IRDCs) (Simon et al. 2006; Rathborne et al. 2006). These could be the star-less objects from which massive stars will form. However, the earliest signs of accretion have also been signposted by directed outflows of cold molecular gas and, it turns out, most of the IRDCs studied so far host weak $24\mu\text{m}$ emission sources and already drive molecular outflows, both strong indicators for active star formation (Rathborne et al. 2010). In addition, the Herschel Space Telescope has helped reveal the full population of early evolutionary stages at the very onset of massive star formation (Beuther et al. 2010; Ragan et al. 2012).

It has been proposed that the large-scale evolution can be split into two phases: an accretion phase and a clean-up phase. Initially, as the protostar gains in mass, its sphere of influence grows, leading to accelerated accretion (McKee & Tan 2003). There is observational support for this as discussed by Davies et al. (2011) which favours either turbulent core (McKee & Tan 2003) or competitive accretion (Bonnell et al. 2001) models. Subsequently, in a distinct second phase, termed the clean-up phase, the accretion has stopped abruptly and the remaining clump material is partly dispersed or integrated into a surrounding cluster (Molinari et al. 2008).

In another scenario, the massive star does not fully form early. Low mass star formation dominates until the clump has considerably evolved. These stars would remain difficult to detect. It has been remarked that the current Initial Mass Function implies two peaks of star formation with the majority of low mass stars forming first and high mass stars forming later (Behrend & Maeder 2001). In competitive accretion, gas is funnelling down to the cloud centre where stars, initially accreting gas with low relative velocity, already have large mass before accreting the late-arriving higher velocity gas (Bonnell & Bate 2006).

Stellar collisions and mergers could supplement gas accretion (Bonnell & Bate 2002). Massive stars could form via coalescence of intermediate mass stars within very dense systems. Although not considered here, along with other scenarios involving fragmentation, these should lead to alternative predictions.

Do high-mass stars form in a scaled-up analogue of the low-mass formation scenario? Molinari et al. (2008) find a consistent interpretation in favour of an analogy. They analysed wide Spectral Energy Distributions (SEDs) to derive bolometric luminosity (L_{bol}) and clump mass (M_{clump}). This leads to the diagnostic diagram of L_{bol} versus M_{clump} (we have replaced the term envelope with clump here, employing envelope to refer to the inner part of the clump which accretes directly on to the protostar). The high-mass objects were then shown to occupy a sequence of regions on this diagram in a similar manner to those evolving Classes which populate the low-mass regions. Herschel data have recently extended this to include protostars (e.g. Elia et al. 2010).

The SED parameters now available include fluxes derived from the Red MSX Source survey, Spitzer IRAC

and MIPS, SOFIA FORCAST, Herschel PACS, Herschel SPIRE, and BLAST. Further data are available across the radio, sub-millimetre and infrared. From these, we can derive clump mass, temperature, luminosity, ultraviolet flux, outflow mass and outflow power. So we can now construct several diagrams to employ as diagnostic tools to estimate the evolutionary stages.

The bolometric luminosity and temperature, T_{bol} , have been used in isolation to test accretion models for a version of the model tuned to low-mass protostars (Froebrich et al. 2006). A similar approach but just using the luminosity function was adopted by Davies et al. (2011) for high-mass stars using MSX data and radio identifications to distinguish protostars from later stages. In place of an SED derivation of luminosity, the $21\mu\text{m}$ flux was utilised with the assumption that the bolometric luminosity can be taken as a reliable proxy for the set of protostars being investigated. Both these approaches led to constraints on the time scale of young stars and the general form of the accretion process.

A potential test would use the radio luminosity, L_r , produced by free-free emission after extreme ultraviolet excitation. The ratio of L_r/L_{bol} should then provide a measure of the development while L_{bol}/M_{clump} provides a distinct measure. Plotted together, such a diagram provides a *distance independent* distribution of evolutionary phases.

Outflow parameters have also been used to distinguish the phases of low-mass stars where accretion is known to decelerate rather than accelerate with time (Caratti o Garatti et al. 2006). This leads to a decrease in the force of the outflow as the source ages (Curtis et al. 2010). Beuther et al. (2002) showed that bipolar outflows are indeed ubiquitous phenomena in the formation process of massive stars, suggesting similar flow-formation scenarios for all masses, consistent again with scaled-up, but otherwise similar, physical processes - mainly accretion - to their low-mass counterparts. Going further, it was shown that the measured molecular hydrogen outflow luminosity is tightly related to the source bolometric luminosity for low mass stars (Caratti o Garatti et al. 2006), and this relationship extends to massive objects (Caratti o Garatti et al. 2008). It is clear that this only applies to the youngest protostars in which the bolometric luminosity is dominated by the release of energy through accretion. Those sources associated with jets are very young (well before the Main Sequence turn-on), while those without detectable jets possess ultracompact H II regions (Beuther & Shepherd 2005; Ramsay et al. 2011).

The objectives of this first paper is to set up the model framework and consider the effects of radiation feedback. We impose simple accretion rates that slowly vary. Subsequent works will tackle accretion outbursts, the outflow properties and the strength of feedback in self-regulation.

The accelerated-accretion model generates a particular L_{bol} versus M_{clump} relation (Molinari et al. 2008). We begin here by exploring how general this is. A constant accretion rate is a common working assumption while there is evidence for both a declining rate as well as a sporadic/episodic rate. These models involve less dramatic cut-offs in the accretion and should generate models with different statistical properties.

A major issue to address later is the existence of two distinct phases. If accelerated accretion is followed by a clean-

up phase, we expect the outflow feedback phase to precede the radiative feedback phase. It may prove difficult for accretion phenomena to still dominate once the rapid rise in ultraviolet flux has started at late times. Quite remarkably, nature has no problem: all of the sources with infall signatures onto Ultracompact H II regions have corresponding outflow signatures as well (Klaassen et al. 2011). This observation suggests that accretion may continue, consistent with the gravo-turbulent model (Schmeja & Klessen 2004). However, both accretion and collimated outflows are probably weak when the star has advanced to its Ultracompact H II stage (Varricatt et al. 2010). An ultimate aim of this study will therefore be to determine the conditions under which the accretion-outflow phase can significantly overlap with the UV phase, associated with the final contraction of a massive star.

2 METHOD

2.1 Model construction: mass movement

The model is constructed upon (1) the extension of the Unification Scheme for low-mass stars, (2) the strategy and model invoked for high-mass stars, (3) the detailed evolutionary tracks of an accreting massive protostar, (4) the results for a range of potential accretion rates and (5) predicted outcomes for radiative and outflow feedback. All algorithms and graphics are written and processed in IDL.

The first task is the construction of a model for the environment in which a given clump mass, M_{clump} , is redistributed in time according to a prescribed formula, constrained by mass conservation. The clump directly supplies three entities: an inner envelope, M_{env} , a surrounding cluster M_{stars} and dispersal into the ambient cloud M_{gas} (with some additional help from the jet-driven outflow). The inner envelope is here assumed to supply the accretion disk at a rate $\dot{M}_{acc}(t)$ which, feeds instantaneously both the star, M_* , and the jets, M_{jets} . The jet material accumulates in an inner outflow, M_{out} , which also pushes out a fraction of the clump. Hence:

$$\dot{M}_{clump}(t) + \dot{M}_{env}(t) + \dot{M}_{stars}(t) + \dot{M}_{gas}(t) = 0, \quad (1)$$

$$-\dot{M}_{env}(t) = \dot{M}_{acc}(t) = \dot{M}_*(t) + \dot{M}_{jets}(t). \quad (2)$$

We will consider two important free parameters. The most critical is the fraction, ξ , of the initial clump mass which ends up as part of the star. Even for low mass stars, it is well known that there must be a much larger obscuring mass than necessary to form the star (Myers et al. 1998). This mass prolongs the embedded phase and extends the late Class 0 and early Class 1 stages. The best estimate for the excess mass was found to be a factor of two in the low-mass version of the present scheme on using accretion rates derived from gravo-turbulent models (Froeblich et al. 2006).

Also for high-mass protostars, the surrounding bound clumps are estimated to exceed the star's mass by a factor which can exceed 30 (Molinari et al. 2008). We thus anticipate quite low values for ξ . Hence, in this work, we assume that the clump mass is sufficient to form the protostar and the associated stellar cluster (see Sub-section 3.1) in addition to gas expelled directly from the clump. We assume both mass loss rates to be constant with the same time scale.

The second parameter is the fractional efficiency ϵ of mass diversion from inflow to outflow, from the disk to the jets. The extended magneto-centrifugal model is expected to be quite efficient and the X-wind model is expected to reach the thirty per cent level (Shu et al. 1988, 1994). In doing so, such magneto-centrifugal mechanisms can carry away the total angular momentum and kinetic energy of the accreting disk material.

Previously, we found that a constant efficiency ϵ was inconsistent with the observations of low-mass stars (Smith 2000). Hence we took

$$\epsilon(t) = \eta \left[\frac{\dot{M}_{acc}(t)}{\dot{M}_o} \right]^\zeta, \quad (3)$$

where \dot{M}_o is the peak accretion rate and ζ is a constant.

The variable jet efficiency was introduced in order to account for evolving outflow properties of low-mass protostars. The Class 0 outflows appear to have a mechanical luminosity of order of the bolometric luminosity of the protostellar core. On the other hand, Class 1 outflows have mechanical luminosities and momentum flow rates up to a factor of 10 lower (Bontemps et al. 1996; Caratti o Garatti et al. 2006). With the same mass outflow efficiency, $\zeta = 0$, this would then require that the *jet speed* is higher in Class 0 outflows. This is, however, contrary to the observations which associate lower velocities ($\sim 100 \text{ km s}^{-1}$) to the Class 0 outflows. Here, we shall assume a constant outflow mass fraction, taking the case $\epsilon = 0.3$ throughout this work.

In general, the mass left over which accretes on to the core to form the star is

$$M_*(t) = \int_0^t (1 - \epsilon(t)) \dot{M}_{acc}(t) dt. \quad (4)$$

2.2 Model construction: accretion rates

The mass accretion rate $\dot{M}_{acc}(t)$ is the main prescribed parameter. We choose the four forms as shown in Fig. 1 and set out below. Note that the power-law and exponential models both include a significant phase of accelerated accretion prior to the prolonged decline.

2.2.1 Constant rate models

Constant accretion models were favoured following the work of Shu (1977) on singular isothermal spheres. It is clear, however, that the rate must eventually fall (by the pre-main sequence stage for low-mass stars) as the reservoir becomes exhausted. Here we assume a constant rate until a cut-off time, t_o , at which the accretion is abruptly halted.

More generally, the collapse of isothermal isotropic cores supported by thermal pressure yields infall rates of the form $\dot{M}_{acc} = f(t) [c_s^3/G]$ where c_s is the sound speed (Foster & Chevalier 1993). The function $f(t)$ can be anything from gradually decreasing over a time $\sim 200\tau$ to a sharply peaked function at time $\sim 0.1\tau$ where the time and mass flow scales are

$$\tau = 1/\sqrt{(4\pi G\rho_c)} = 1.3 \cdot 10^5 \left[\frac{7.6 \cdot 10^{-20} \text{ g cm}^{-3}}{\rho_c} \right]^{1/2} \text{ yr} \quad (5)$$

and

$$\frac{c_s^3}{G} = 1.6 \cdot 10^{-6} \left[\frac{c_s}{0.19 \text{ km s}^{-1}} \right]^3 \text{ M}_\odot \text{ yr}^{-1}, \quad (6)$$

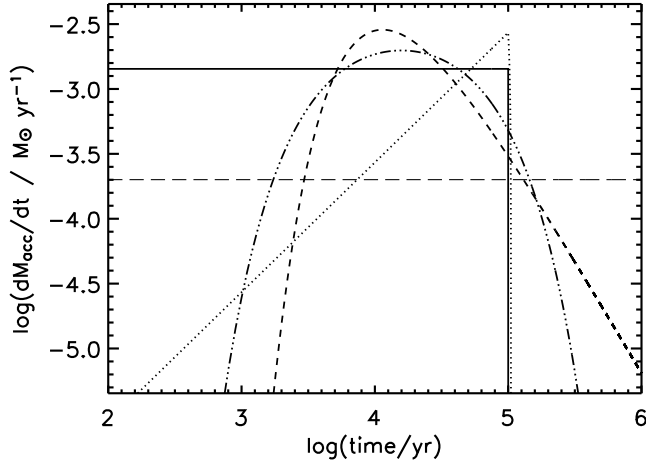


Figure 1. Accretion rates as a function of time (log-log plot). The rate of loss of mass from the envelope is displayed for the five models discussed in the text. In each case a star of mass $100 M_{\odot}$ is formed on assuming 30% of the envelope mass is ejected in jets. The models are (i) constant fast accretion for 10^5 yr (solid line), (ii) constant slow accretion for $\times 10^6$ yr (long-dashed), (iii) power law with maximum $\dot{M}_{acc} = 4.01 \times 10^{-3} M_{\odot} \text{ yr}^{-1}$ (dashed), (iv) exponential with maximum $\dot{M}_{acc} = 2.77 \times 10^{-3} M_{\odot} \text{ yr}^{-1}$ (dot-dashed), and (v) accelerated accretion for 10^5 yr (dotted line).

where ρ_c is the initial central density. Inclusion of envelope spin, turbulence, magnetic field and fragmentation would introduce further initial parameters (see review by Larson (2003)).

2.2.2 Exponential models

One type of model assumes the envelope loses mass in proportional to its mass, $\dot{M}_{acc} = -\dot{M}_{env} \propto M_{env}$ (Bontemps et al. 1996; Myers et al. 1998). This leads to an exponentially decreasing envelope mass

$$M_{env}(t) = M_o e^{-t/\tau_f}, \quad (7)$$

and an accretion rate

$$\dot{M}_{acc}(t) = \frac{M_o}{t_f} e^{-t/\tau_f}, \quad (8)$$

which thus begins with an established high accretion rate. A modified exponential model allows for a rapid rise and fall by modelling

$$\dot{M}_{acc}(t) = \dot{M}_o e^{2(\tau_r/\tau_f)^{1/2}} e^{-\tau_r/t} e^{-t/\tau_f}, \quad (9)$$

and we can put $\tau_r = 0$ if desired. The maximum accretion rate \dot{M}_o occurs at time $t_m = \sqrt{(\tau_r \tau_f)}$.

2.2.3 Power law models

The favoured model for low-mass evolution involves a sharp exponential rise followed by a prolonged power law decrease in time (Smith 1999, 2000). The power-law has substantial observational support (Calvet et al. 2000). The early peak may reach $\dot{M}_{acc} = 10^{-4} M_{\odot} \text{ yr}^{-1}$ for 10^4 years, and eventually fall to $\dot{M}_{acc} = 10^{-7} M_{\odot} \text{ yr}^{-1}$ for 10^6 years, corresponding to Class 0 and Class 2 or Classical T Tauri stars, respectively.

We choose the accretion rate to take the form

$$\dot{M}_{acc}(t) = \dot{M}_o \left(\frac{e}{\alpha}\right)^{\alpha} \left(\frac{t}{t_o}\right)^{-\alpha} e^{-t_o/t}. \quad (10)$$

Note that we can choose α to simulate various models: an asymptotic constant-accretion model corresponds to $\alpha \sim 0$ and t_o small, gradual-accretion corresponds to $\alpha \sim 0.5$ and abrupt accretion to $\alpha \sim 2-3$. In this work, we take $\alpha = 1.75$ as a default value. The envelope evolution can be written analytically in terms of an incomplete Gamma function on integrating Eqn. 10:

$$M_{env}(t) = \dot{M}_o t_o (e/\alpha)^{\alpha} [1 - \Gamma(\alpha - 1, t_o/t)]. \quad (11)$$

2.2.4 Accelerated accretion

A power-law form for the accretion rate, in which the star's growth accelerates, takes a simple form:

$$\dot{M}_{acc}(t) = \dot{M}_o \left(\frac{t}{t_o}\right)^n, \quad (12)$$

for $t < t_o$ with the final, maximum rate \dot{M}_o . The accretion in this case is assumed to be $\dot{M}_{acc} = 0$ for $t > t_o$. This yields a final mass for the star of

$$M_f = \frac{\dot{M}_o t_o (1 - \epsilon)}{1 + n}, \quad (13)$$

assuming ϵ is constant.

The sudden drop in the accretion rate at $t = t_o$ appears as a sharp spike in $L - M$ plots since the contribution to the bolometric luminosity from the accretion luminosity disappears. This can be seen in the tracks calculated by Molinari et al. (2008). Here, we include a brief period of linear decline down to a minimum accretion rate of $10^{-4} \dot{M}_o$:

$$\dot{M}_{acc}(t) = 20 \times \dot{M}_o (1.05 - t/t_o) \quad (14)$$

for $t_o < t < 1.05 t_o$.

The turbulent core model is reproduced with $n = 1$ which leads to $\dot{M}_* \propto M_*^{1/2}$. This model has been shown to lead to some predictions which are consistent with different sets of data (Molinari et al. 2008; Davies et al. 2011).

Note that observed correlations between accretion rates and mass such as $\dot{M}_{acc} \propto M_*^{1.8 \pm 0.2}$ (Natta et al. 2006) apply to a relatively mature stage of young stars. In contrast, $\dot{M}_{acc} \propto M_*^1$ was uncovered (Barentsen et al. 2011; Spezzi et al. 2012). However, it is no surprise that the results differ according to the precise sample selection criteria

2.3 Growth of the star

The structure of a protostar while it accretes at a constant rate has been calculated by Hosokawa & Omukai (2009) in the ‘Hot Accretion’ scenario corresponding to spherical free-fall. If, instead of free-fall on to the surface, the gas settles via an accretion disk, the ‘Cold Accretion’ structure is appropriate (Hosokawa et al. 2010). In the Hot Accretion case, the stellar radius swells up to over $100 R_{\odot}$ for $\dot{M}_* > 10^{-3} M_{\odot} \text{ yr}^{-1}$. The accretion may continue until after the arrival on the Main Sequence, arriving at higher masses for higher accretion rates.

For this work, we have fitted analytical functions to the template figures provided in the above two studies for the radius, R_* , and luminosity, L_* . The four functions correspond

to the four main stages with smooth interpolation between these stages. The stages are (1) the adiabatic accretion, (2) the swelling (or bloating), (3) the Kelvin-Helmholtz contraction and, finally, (4) main-sequence accretion. The resulting functions are shown in Figs. 2 and 3. Figure 3 displays both the accretion and stellar luminosities, and demonstrates that the accretion luminosity dominates until the radial swelling stage which is apparent as a dip in the bolometric luminosity.

The stellar structure depends on the stellar mass, the initial interior state and the accretion rate history. For the case of a constant accretion rate, the above published works provide accurate templates for fiducial cases. However, to employ these figures for time-varying accretion, Davies et al. (2011) took the current accretion rate to look up the radius and luminosity from Hosokawa & Omukai (2009). This method may be a reasonable approximation when the accretion rate continues to increase such that most of the mass has been accumulated within a factor of two of the present accretion rate. More accurately for the adiabatic phases, we here calculate how the star has accumulated the mass and entropy over its entire evolution. Thus a mass-averaged accretion rate, proportional to the accumulated entropy, is employed. However, this method would still lead to very large errors when the accretion rate varies by large amounts, decreases considerably or varies rapidly in the post-adiabatic stages.

When the above method yields a Kelvin-Helmholtz time that is comparable or shorter than the accretion time scale, the adiabatic approximation is invalid. A compromise solution would employ both the current and the mass-averaged accretion rates so as to deliver the correct stellar parameters for the two limiting cases of adiabatic accretion and rapid loss of entropy. This is parameterised with the use of the factor $f = t_{acc}/t_{KH}$ where, as usually defined, $t_{acc} = M/\dot{M}$ and $t_{KH} = GM^2/(RL_{int})$, as determined by the mass-averaged accretion rate. We then take this factor to determine the stellar radius and luminosity relative to the mass averaged values, R_o , L_o , by the additive factors $(1 - exp(-f)) \times (R(t) - R_o)$ where $R(t)$ is the stellar radius calculated from the current rate. While this compromise is more accurate, this would still lead to spurious properties if accretion variations are very rapid.

In this paper, therefore, we will use a second method, where the structure at any time is determined by the mass-averaged accretion rate over the history of the star limited to the past Kelvin-Helmholtz time. We implement an iterative process to determine the radius, luminosity and mass-average accretion rate since these are themselves functions of t_{KH} . Upon testing, we find that the maximum difference between the two methods is typically a few per cent and occurs in the Kelvin-Helmholtz phase. In comparison, simply assuming the current accretion rate and reading the stellar structure from the constant-rate simulations, generated errors of order of 10% in radius throughout the first three evolutionary stages for the slowly varying rates displayed in Fig. 1. Although not ideal, it could still be implemented for most present purposes.

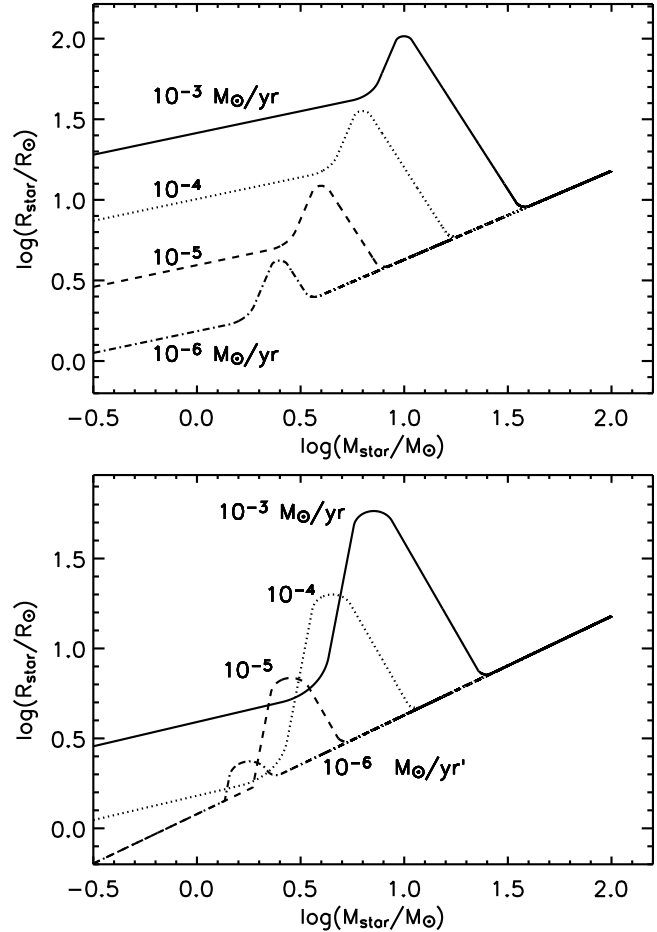


Figure 2. Stellar radius evolution for Hot Accretion (upper panel) and Cold Accretion (lower panel). The mass is accreted for four constant accretion rates, \dot{M}_* , as indicated. These were calculated from analytical approximations to the data presented by Hosokawa & Omukai (2009) for the case of hot accretion and Hosokawa et al. (2010) for the case of cold accretion.

2.4 Radiation feedback modelling

The bolometric luminosity, L_{bol} , and the jets' mechanical power, P_{jets} , are equated to the gravitational energy released through accretion and the stellar luminosity:

$$L_{bol} + P_{jets} = L_{acc} + L_* + P_{jets} = \frac{M\dot{M}_{acc}}{R_*} + L_*. \quad (15)$$

The jets' power is related to the jet mass outflow and accretion rates by

$$P_{jets} = \frac{1}{2}\dot{M}_{jets}v_{jet}^2 = \frac{1}{2}\epsilon\dot{M}_{acc}v_{jet}^2. \quad (16)$$

We take

$$v_{jet}^2 = \chi^2 \frac{GM_*}{R_*}, \quad (17)$$

with $\chi = 1$ as the default constant value, corresponding to a jet speed proportional to the escape speed from the stellar surface.

The accretion luminosity is thus

$$L_{acc} = (1 - \frac{1}{2}\chi^2\epsilon) \frac{M\dot{M}_{acc}}{R_*}. \quad (18)$$

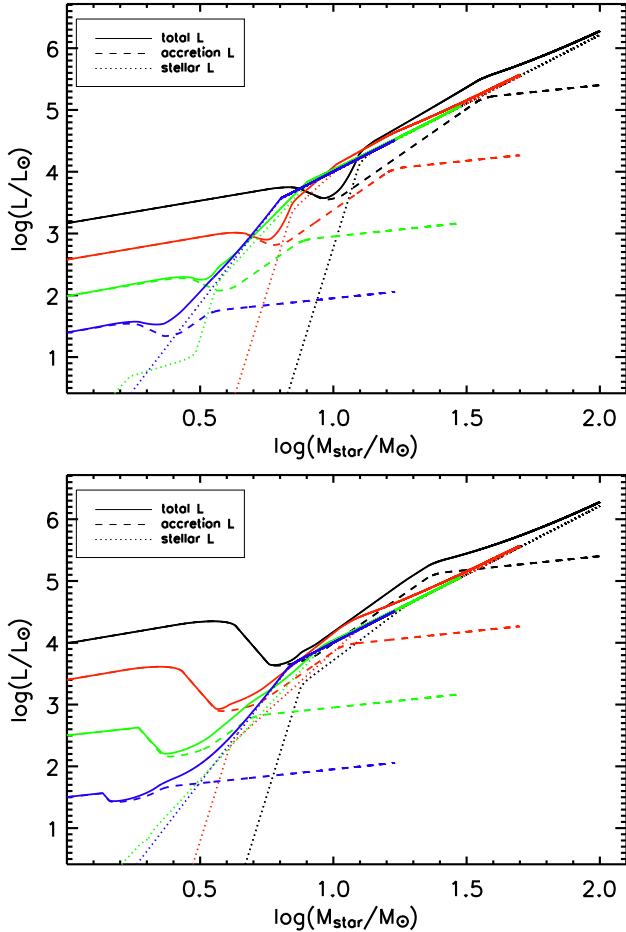


Figure 3. Luminosity evolution for Hot Accretion (upper panel) and Cold Accretion (lower panel). The total (solid), accretion (dotted) and stellar (dashed) luminosities are displayed for four constant accretion rates, \dot{M}_* , creating stars of final mass M_f with $\dot{M}_* = 10^{-3} M_{\odot} \text{yr}^{-1}$ and $M_f = 100 M_{\odot}$ (black lines), $\dot{M}_* = 10^{-4} M_{\odot} \text{yr}^{-1}$ and $M_f = 50 M_{\odot}$ (red lines), $\dot{M}_* = 10^{-5} M_{\odot} \text{yr}^{-1}$ and $M_f = 30 M_{\odot}$ (green lines), and $\dot{M}_* = 10^{-6} M_{\odot} \text{yr}^{-1}$ and $M_f = 17 M_{\odot}$ (blue lines), calculated from analytical approximations to the data presented by Hosokawa & Omukai (2009) (hot accretion) and Hosokawa et al. (2010) (cold accretion).

It should be noted that this remains an approximation since various factors, such as stellar rotation, are not accounted for.

The radiation feedback into the environment consists of an ionizing effect and a heating effect on the surrounding envelope. The ultraviolet Lyman flux from the protostar and the accreting material ionizes the environment, generating an H II region. This region can be observed in the radio continuum through free-free emission.

The Lyman flux was tabulated in the work of Davies et al. (2011) for hot main sequence stars. This provides an excellent up-to-date blueprint for stars evolving on to the Main Sequence although expected uncertainties remain very high. Since they considered that significant Lyman flux in their sample would only occur when the star was as good as on the Main Sequence, they were able to directly use their tabulated values given the stellar mass. In the present study, we have calculated approximations to

the Lyman flux based on the work of Panagia (1973) and Davies et al. (2011) to relate surface temperature to the Lyman flux, and then employed the stellar temperature and radius to determine the flux of Lyman photons. We find that the two works are in close agreement and power-law approximations appropriately represent them. In detail, the fit used is $L_{Ly} = 4\pi R_*^2 F_{Ly}$ with

$$\log(F_{Ly}) = 23.14 + 15.8(\log(T_*) - 4.5) \quad \log(T_*) < 4.55 \quad (19)$$

$$\log(F_{Ly}) = 24.7 + 5.1(\log(T_*) - 4.7), \quad \log(T_*) > 4.55. \quad (20)$$

To convert a predicted ultraviolet Lyman flux into a high-frequency radio flux density is straightforward. Provided the observed region is ionisation bounded and the frequency is sufficiently high to ensure that self-absorption is negligible, then the two are approximately proportional (Rubin 1968; Sánchez-Monge et al. 2013):

$$\frac{N_{Ly}}{\text{counts s}^{-1}} = 43.6 \left(\frac{S_{5GHz}}{\text{mJy}} \right) \left(\frac{D}{\text{kpc}} \right)^2, \quad (21)$$

which yields

$$\frac{L_{Ly}}{L_{\odot}} = -0.63 \left(\frac{S_{5GHz}}{\text{mJy}} \right) \left(\frac{D}{\text{kpc}} \right)^2. \quad (22)$$

2.5 Envelope & bolometric temperature

The observed spectral energy distributions of protostars are often complex with multiple peaks. In this work, we restrict the analysis to predicting the bolometric temperature of the optically-thick core of the clump given a spherically-symmetric model. This provides an indication of how the peak wavelength will change with age. However, this should be only considered indicative since, even in this homogeneous spherically symmetric approximation, we require several other major assertions concerning the gas and dust distribution.

We consider two methods corresponding to different clump detection and measurement scenarios. In Method 1, we first set up a large clump of mass M_{clump} with a mass related to the most massive star (see Equation 34 below) with a radial power-law density distribution. This clump model was explored by Froebrich et al. (2006), and the sensitivity to parameter ranges was tested. Following those results, we take a small fixed inner envelope radius, R_{in} , of 30 AU, in order to sustain a high accretion rate. We calculate an optical depth of the clump τ_c assuming a spherical density structure with $\rho \propto R^{-\beta}$. The outer clump radius, R_{out} , is taken to be located where the clump merges into the ambient cloud, i.e. where the temperature has fallen to that of the ambient molecular cloud, taken here as 12 K. The inner clump density is then

$$\rho_{in} = \frac{(3 - \beta)M_{clump}}{4\pi R_{in}^3 \zeta} \quad (23)$$

where $\zeta = (R_{out}/R_{in})^{(3-\beta)} - 1$, and the clump optical depth is

$$\tau_c = \kappa \rho_{in} R_{in} \frac{1 - \zeta^{1-\beta}}{\beta - 1}. \quad (24)$$

We follow Myers et al (1998) and take the emissivity at $12\mu\text{m}$ as $\kappa = 4 \text{ cm}^2 \text{ g}^{-1}$.

The inner temperature of the clump is

$$T_{in}(t) = \left[\frac{L_{bol}(t)}{4\pi \cdot \sigma \cdot R_{in}^2} \right]^{1/4}. \quad (25)$$

This yields an optical depth through the envelope proportional to the emissivity:

$$\tau_c(t) = \kappa \cdot \rho_{in}(t) \cdot R_{in} \cdot \frac{1 - \zeta(t)^{1-\beta}}{\beta - 1}. \quad (26)$$

Following Myers et al. (1998), we take $A = 1.59 \cdot 10^{-13} \text{ cm}^2 \text{ g}^{-1} \text{ Hz}^{-1}$, h as the Planck constant, k the Boltzmann constant, and calculate the bolometric temperature from

$$T_{bol}(t) = \frac{\Gamma(9/2) \cdot \zeta(9/2)}{\Gamma(5) \cdot \zeta(5)} \cdot \left[\frac{h \cdot \kappa \cdot T_{in}(t)}{k \cdot A \cdot \tau_c(t)} \right]^{1/2}. \quad (27)$$

The above Method 1 was devised for the low-mass protostellar case in which the clump is described as a core, and its mass may correspond to that of the enhanced density and temperature which distinguishes it from the embedding molecular cloud. This case leads to linear isotherms on the diagnostic L_{bol} - M_{clump} logarithmic diagrams with the bolometric temperature simply proportional to M_{clump} / L_{bol} for the case $\beta = 1.5$. As shown in the top panel of Fig. 4, the predicted isotherms are quite close together thus requiring a wide range of bolometric temperatures to cover the data for the displayed Herschel clumps.

In the high-mass case, we associate the clump with a size that is only mildly dependent on the clump mass. The observed median half-size is $5 \times 10^4 \text{ AU}$ (Molinari et al. 2008; Veneziani et al. 2013). Here, we will assume this value as a constant outer radius with larger clumps having the extra mass ‘squeezed in’, as concluded by Beuther et al. (2013). To complete the model for Method 2, the inner radius, R_{in} , of the clump is taken to be the sublimation radius i.e. $T_{in} = 1,400 \text{ K}$. With these two boundary conditions replacing those of Method 1 (the distribution otherwise the same as described above), this Method 2 yields well-separated isotherms as shown in the lower panel of Fig. 4. We will display isotherms derived from Method 2 in the following.

2.6 Disk accretion

At the inner radius, the envelope feeds a circumstellar disk. We assume here, and will test in a following study, the working assumption that the disk is ‘viscous’ and steady, and that the gas spends relatively little time in the disk and so reaches an inner accretion disk at the same rate as with which it is supplied by the envelope. The inner accretion may be non-steady, the gas either being expelled in the jets or accumulated onto the surface of the protostar, later to become the star itself. The disk mass is thus proportional to the accretion rate and the accretion time scale.

Standard turbulent viscosity is efficient at separating the flux of angular momentum from the mass out to radii of about 100 AU for the initial rapid accretion rates from the envelope. Hence massive outer disks could build up until the viscous mechanisms associated with self gravity are effective. This could lead to the formation of secondary objects (stars, brown dwarfs), and so cut off both the star and jet supply line. Perhaps more likely is that high accretion rates lead to simultaneous binary formation and powerful molecular jets.

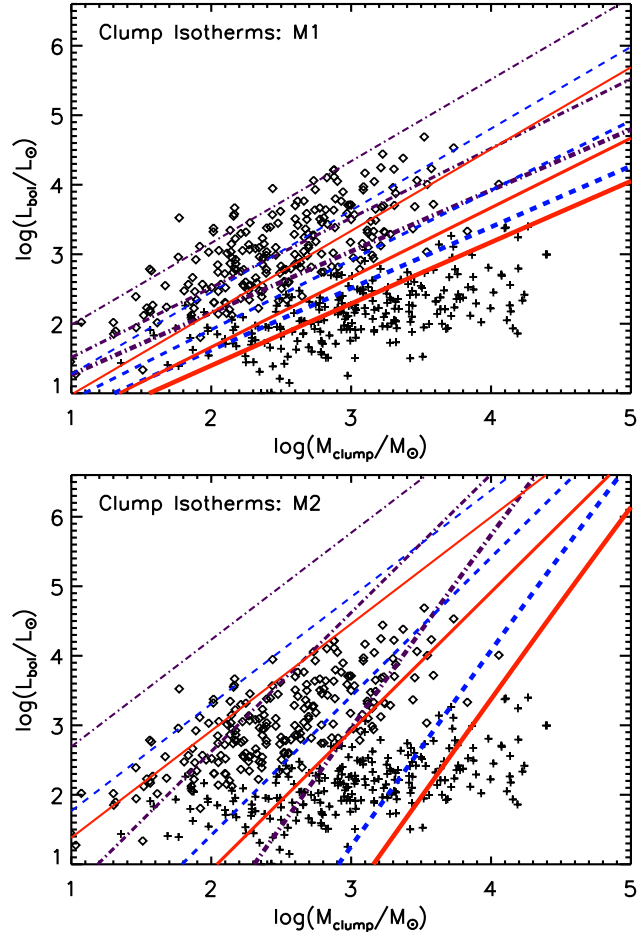


Figure 4. Isotherms for the bolometric temperature of clumps plotted on the L_{bol} - M_{clump} diagram. The upper panel employs Method 1 with a fixed inner radius of 30 AU and an outer radius of temperature 12 K while Method 2 is displayed in the lower panel where the inner radius is determined by dust sublimation and the outer radius is a constant of 50,000 AU (i.e. full size of 0.5 pc). The isotherms are for temperatures of 15 K (full red), 30 K (dashed blue) and 45 K (dot-dash black) with $\beta = 1.2$ (lower thick), 1.5 and 1.8 (upper thin). The data are from the Herschel $l = 30^\circ$ field as analysed by Veneziani et al. (2013) with protostellar clumps (diamonds) and pre-stellar clumps (crosses, taken as clumps with no detected stars but which are gravitationally bound if the temperature is used to derive the relevant internal measure of pressure).

We assume here that the inner disk processes the material fast and so remains steady. The outer part of the disk will lag behind. The outer radius of the steady state disk can be found by requiring the disk accretion time scale $t_\nu(R) = R^2/\nu$ to be less than the time scale for changes in the accretion rate $\dot{M}_{acc}/\dot{M}_{acc}$. This yields a steady disk extent R_s .

The disk temperature T_d and sound speed c_d are given by standard expressions for an optically thick and isothermal structure (Pringle 1981). The accretion energy is radiated locally:

$$T_d^4(R, t) = \frac{3GM(R, t)\dot{M}_a(t)}{8\pi\sigma R^3} \left[1 - \left(\frac{R_*}{R} \right)^{\frac{1}{2}} \right], \quad (28)$$

where $M(R, t) = M_*(t) + M_d(R, t)$ is the sum of the protostellar and disk mass internal to R . The sound speed for a molecular gas disk with a mean molecular weight of 2.3 is $c_d = 6.01 \cdot 10^3 T_d^{1/2} \text{ cm s}^{-1}$.

The disk mass M_d is not expressible analytically since the accretion is driven by two viscosity components with differing functional forms. First, we take the usual turbulent viscosity $\nu_t = \alpha_d c_d H$ where H is the disk thickness and α_d is a dimensionless parameter which we set to 0.1 unless otherwise stated (Shakura & Sunyaev 1973). This yields

$$\nu_t = \frac{2 \alpha_d c_d^2}{3 \Omega}, \quad (29)$$

where the angular rotation speed is $\Omega = \sqrt{(GM/R^3)}$. The component of viscosity related to self-gravitational forces is parameterised, as suggested by Lin & Pringle (1987):

$$\nu_g = \frac{2 \mu_d c_d^2}{3 \Omega} \left(\frac{Q_c^2}{Q_t^2} - 1 \right) \quad (30)$$

for $Q_t < Q_c$ and $\nu_g = 0$ otherwise. Here, the efficiency parameter μ_d and the instability parameter Q_c will also be set to unity (see Lin & Pringle (1990)). Hence, the parameter

$$Q_t = \frac{c_d \Omega}{\pi G \Sigma} \quad (31)$$

determines the importance of viscosity through the disk's own gravity. Note that the viscosity can be determined by self-gravity even when the protostellar mass is large when the disk column density is large. This may well arise where the turbulent viscosity is inefficient, in the outer disk regions, leading to a build up of mass until self-gravity takes effect.

The disk column density is given by

$$\Sigma = \frac{1}{2\pi R} \frac{dM}{dR} \quad (32)$$

and the cumulative mass distribution

$$\frac{dM}{dR} = \frac{R \dot{M}_{acc}}{\nu_t + \nu_g} \quad (33)$$

is given by the viscosity. From the disk column it is straightforward to calculate the disk radius at which the optical depth is unity, $R_{\tau=1}$. This completes the set of equations which is integrated from an inner radius to yield the full disk structure. The results for disks associated low-mass protostars were presented by Smith (2000) and will be extended in a following work.

3 RESULTS

3.1 Clump Mass v. Bolometric Luminosity

Cloud mass, bolometric luminosity and bolometric temperature are quantities derived from observations. The bolometric temperature is sensitive to the geometry, orientation and uniformity of the clump. Therefore, the relationship between cloud mass and bolometric luminosity is most often employed as a diagnostic tool for the formation of high-mass stars (Molinari et al. 2008; Beltrán et al. 2013) as well as lower-mass stars (Reipurth et al. 1993; Saraceno et al. 1996; Smith 2000). More recently, $L_{bol}-M_{clump}$ or $L_{bol}/M_{clump}-M_{clump}$ diagrams have been utilised to analyse Herschel Space Telescope data (Elia et al. 2010; Ragan et al. 2012).

To interpret these data points as a time sequence, it

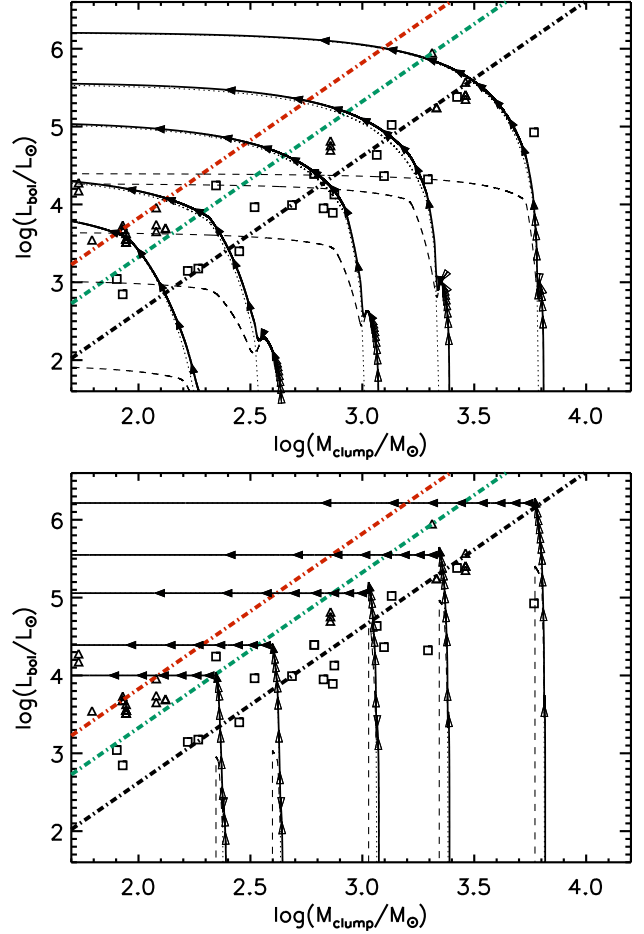


Figure 5. $L_{bol}-M_{clump}$ diagrams for Constant Slow Accretion (simultaneous star and clump evolution, upper panel) and Constant Fast Accretion (early formation of the massive star, lower panel), both forming via hot accretion. The five solid lines correspond to systematically increasing final stellar masses of 10, 15, 30, 50 and $100 M_{\odot}$. Initial clump masses, final stellar mass, accretion timescale and accretion rates are provided in Table 1. The contributing luminosity components derived from accretion (dashed lines) and interior (dotted lines, where visible) are indicated. The filled arrowheads are laid at equal time intervals of one tenth the total time, and the ten unfilled arrowheads are similarly placed in the first of these intervals. For comparison, we overlay (1) the data set presented by Molinari et al. (2008) where the triangles denote the infrared sample while the squares denote the millimetre sample. The three straight dot-dashed lines correspond to bolometric temperatures of 40 K (blue), 60 K (green) and 80 K (red) as calculated by Method 2 with an envelope density radial power-law index of 1.5.

is assumed that the clump mass decreases in time as the luminosity increases (Andre et al. 1993). Model evolutionary tracks are then easily calculated based on the principles discussed in Section 2 upon choosing an accretion type and rate.

The initial clump mass is assumed to be directly related to the final mass of the most massive star, M_{*f} , by the relation

$$\log M_{clump}(0) = A + 1.41 \log M_{*f}. \quad (34)$$

Here, $A = 0.55$ could be taken (Molinari et al. 2008) on

Table 1. Model data employed in Figs. 5 and 6 in forming a $100 M_{\odot}$ star from an initial clump of mass $6,561 M_{\odot}$ (left) and a $10 M_{\odot}$ star from an initial clump of mass $247 M_{\odot}$ (right), all with 30% of the mass ejected through jets or outflow.

Accretion Model	Max. accretion rate $10^{-3} M_{\odot} \text{ yr}^{-1}$	Accretion timescale 10^5 yr	Clump timescale 10^5 yr	Max. accretion rate $10^{-3} M_{\odot} \text{ yr}^{-1}$	Accretion timescale 10^5 yr	Clump timescale 10^5 yr
Constant - Slow	0.141	10.0	10	0.0014	100	100
Constant - Fast	1.413	1.0	10	0.0141	10	100
Accelerated	2.717	1.0	10	0.0907	3	10
Power Law	2.861	0.2	10	0.2861	0.2	10
Exponential	1.980	1.0	10	0.1980	1.0	10

the assumption that the clump generates the bound cluster (Faustini et al. 2009). However, accounting for the global gas escape as well as that from protostellar outflows, we shall take $A = 0.85$ corresponding to a star formation efficiency of 50%. As will be seen below, such high efficiencies are inconsistent and much larger values of A need to be considered.

The clump gas is taken to be reduced at a constant rate (excluding the inner envelope which supplies the massive star). However, other relationships between the stellar cluster and most-massive star have been considered and, above all, there is a wide spread in the measured values of A (Weidner et al. 2010) corresponding to an order of magnitude in mass.

Diagrams for models with constant hot accretion are shown in Fig. 5 and for variable rates in Fig. 6. Also shown are observational data for far-infrared and infrared sources and the theoretical bolometric temperature isotherms. Note that these isotherms as calculated from Equation 27 are in agreement with the bolometric temperatures directly derived in the literature.

The top panel of Fig. 5 displays the tracks for a slow evolution (e.g. Behrend & Maeder 2001) with a simultaneous cloud evolution. This yields a strong dependence between the two parameters with a wide distribution of sources predicted. In recent works, the clump mass is assumed to fall at a slow constant rate with time while the massive star forms abruptly from a compact envelope, which is consistent with both available data and theoretical expectations (McKee & Tan 2002). We therefore discount the Slow Accretion scenario as a model for clump/cluster evolution although it is relevant in following the possible evolution of an isolated core especially in the low-mass case.

The constant Fast Accretion case is shown in the lower panel of Fig. 5. It is clear that massive infrared protostars would be rarer in this case (as indicated by the arrowheads placed at regular time intervals). In addition, a much narrower range in clump masses for a given luminosity interval is predicted in the latter case.

The Accelerated Accretion Model generates similar results (top panel of Fig. 6) with two distinct track stages. This was the model explored by Molinari et al. (2008) but we note here that both the constant and power law fall-off models produce very similar tracks. To differentiate between models will require a detailed statistical analysis. The Power Law Model generates tracks in which there is an extended transition stage between the accretion and clean-up stages

(middle panel of Fig. 6). This transition stage occurs at bolometric temperatures between 60 K and 80 K.

It should also be remarked that the track direction changes from almost vertically up to down for a short period. This is caused by the swelling of the protostar which reduces the bolometric luminosity by reducing the accretion luminosity. While hardly visible in Fig. 6, this effect becomes prominent in the cold accretion scenario where the expansion phase is stronger. This is shown in Fig. 7 for the Power Law Model in which it is most obvious. In general, however, we find that Cold Accretion does not significantly alter the tracks on the $L_{bol}-M_{clump}$ plots.

3.2 Bolometric Temperature

The bolometric isotherms calculated through Method 2 are shown on the $L_{bol}-M_{clump}$ plots. The temperatures are broadly consistent with the range of temperatures derived from the spectral energy distributions for the Herschel sources. We do not expect more than this given the known sensitivity to geometry and orientation. Indeed, as shown in Fig. 4, there is a strong dependence on the radial density distribution as given by the index β .

However, we can compare the accretion models statistically to determine if they would yield significantly different statistics in terms of numbers of source in any temperature interval. These numbers are provided in Table 2. As also illustrated in Fig. 8, there is a remarkable difference between the Accelerated Accretion model and the alternative evolutions. In the Accelerated Accretion Model, significantly more time elapses in the low temperature ($< 30 \text{ K}$) regime. For the $100 M_{\odot}$ case, all the other models investigated (with the exception of Slow Accretion) spend much less time at low temperatures, by a factor of two to three. This result is consistent with expectations: accelerated accretion takes time to get off the ground.

3.3 Herschel Hi-Gal data

Data directly comparable to that predicted in Table 2 are available through several Herschel programmes. The distribution of bolometric temperatures in Table 2 along with the data employed here are inconsistent. Over 80% of observed clumps have temperatures below 30 K (bottom lines in Table 2) whereas the models predict a much more even number distribution with temperature. It is clear that only a small fraction of the Herschel cores on the very high mass tracks will go on to form such massive stars.

Table 2. The fraction of the total time required to reach a bolometric temperature of 100 K in order to traverse the indicated temperature range for the models to form a star of mass $100 M_{\odot}$ through hot (upper section) and cold (lower section) accretion. The clump mass is given by Equation 34 and the radius of the clump is 50,000 AU, consistent with the R_{env} values derived by Molinari et al. (2008). Herschel Hi-Gal fractions are taken from the two fields analysed by Elia et al. (2010) and Veneziani et al. (2013).

Accretion Model	< 20 K	< 30 K	30 K – 50 K	50 K – 70 K	< 100 K time ($\times 1000$ yrs)
HOT ACCRETION:					
Constant - Slow	0.250	0.442	0.279	0.158	866
Constant - Fast	0.027	0.057	0.397	0.356	845
Accelerated	0.058	0.080	0.373	0.356	845
Power Law	0.020	0.049	0.446	0.321	847
Exponential	0.025	0.051	0.402	0.356	845
COLD ACCRETION:					
Constant - Slow	0.250	0.442	0.279	0.158	866
Constant - Fast	0.022	0.057	0.397	0.356	845
Accelerated	0.052	0.080	0.373	0.356	845
Power Law	0.017	0.049	0.446	0.321	847
Exponential	0.021	0.051	0.402	0.356	8459
Hi-Gal Data: (Elia et al 2010)					number
$l = 30^{\circ}$ field	0.463	0.832	0.128	0.022	311
$l = 59^{\circ}$ field	0.417	0.846	0.142	0.011	91
H-Gal YSOs (Veneziani et al 2013)	0.463	0.989	0.011	0	284

Table 3. The fraction of the total time required to reach a bolometric temperature of 100 K in order to traverse the indicated temperature range for cold accretion with fixed clump mass as indicated but different final stellar masses. The radius of the clump is 30,000 AU consistent with the values derived by Veneziani et al. (2013).

Final Stellar Mass	< 20 K	< 30 K	30 K – 50 K	50 K – 70 K	< 100 K time (yrs)
Constant - Fast					
CLUMP MASS: $6,683 M_{\odot}$					
CLUMP RADIUS: 50,000 AU					
100	0.022	0.057	0.396	0.356	845
50	0.042	0.233	0.538	0.148	929
30	0.077	0.581	0.294	0.081	960
15	0.550	0.810	0.133	0.036	1472
10	0.715	0.880	0.084	0.023	988
CLUMP MASS: $5,740 M_{\odot}$					
CLUMP RADIUS: 30,000 AU					
STELLAR MASS: $30 M_{\odot}$					
Constant - Slow	0.672	0.826	0.114	0.037	2,936
Constant - Fast	0.473	0.778	0.156	0.043	2,935
Accelerated	0.473	0.777	0.156	0.043	978
Power Law	0.497	0.781	0.153	0.042	978
Exponential	0.472	0.777	0.156	0.043	978
Hi-Gal Data:					number
$l = 30^{\circ}$ field	0.463	0.832	0.128	0.022	311
$l = 59^{\circ}$ field	0.417	0.846	0.142	0.011	91
H-Gal YSOs (Veneziani et al 2013)	0.463	0.989	0.011	0	284

A resolution to this problem is straightforward: the most massive forming star observed in the clumps is a factor of about 3 smaller than that used in the literature to calculate tracks. In Table 3, we present re-calculated number distributions on the assumption that the clump masses are indeed large but are actually being heated by protostars which will form much lower mass stars. The new tracks are illustrated in Fig. 10. Extremely good correspondences are

apparent. Note that the initial clump masses are now 4.7 times larger, corresponding to stars of three times the mass according to Equation 34.

This interpretation of the statistics, in which only 10–15% of the initial clump mass ends up in stars, is independent of the accretion model. As shown on the panels of Fig. 9, it is very difficult to distinguish between the models for the high mass clumps.

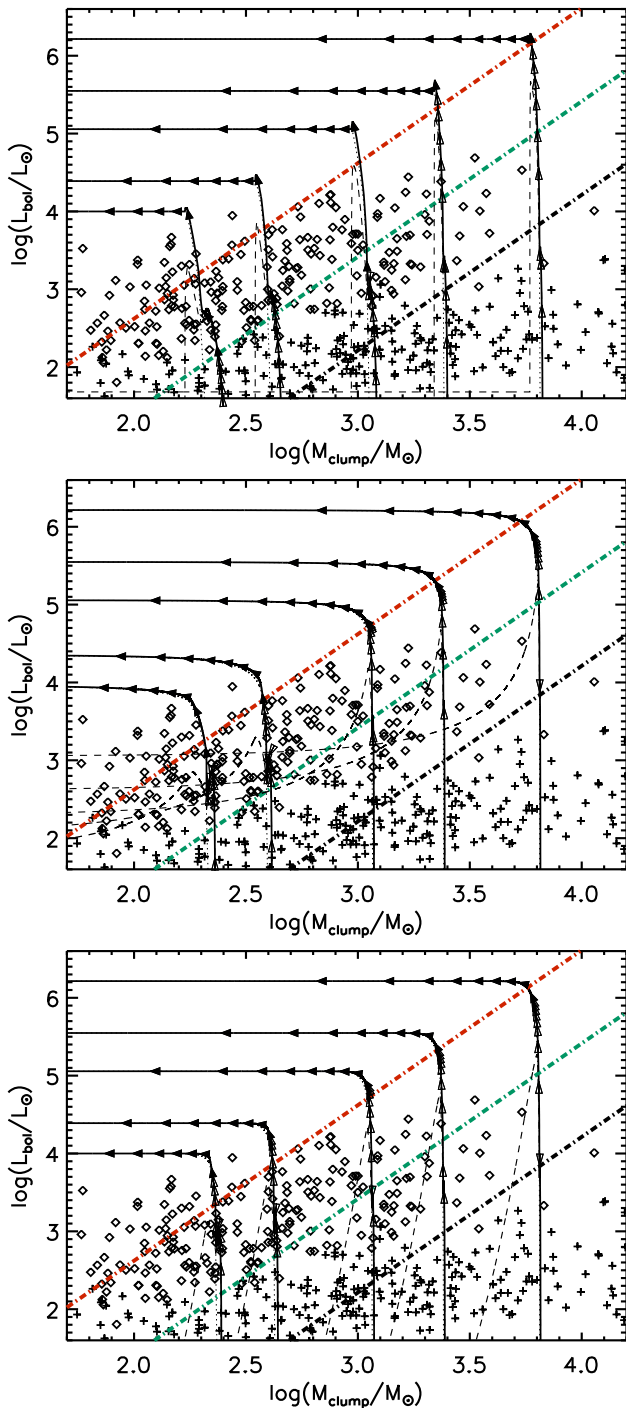


Figure 6. L_{bol} - M_{clump} diagrams for Accelerated (upper), Power Law (middle) and Exponential (lower panel) accretion models assuming hot accretion. The model parameters are provided in Table 1. The data are the set of Herschel objects from the $l = 30^\circ$ field from the Herschel Infrared GALactic plane survey (HiGal) (Elia et al. 2010) as revised by Veneziani et al. (2013). The three straight lines correspond to bolometric temperatures of 10 K (blue), 20 K (green) and 40 K (red) as calculated by Method 2 with an envelope density radial power-law index of 1.5. See the caption of Fig. 5 for other details.

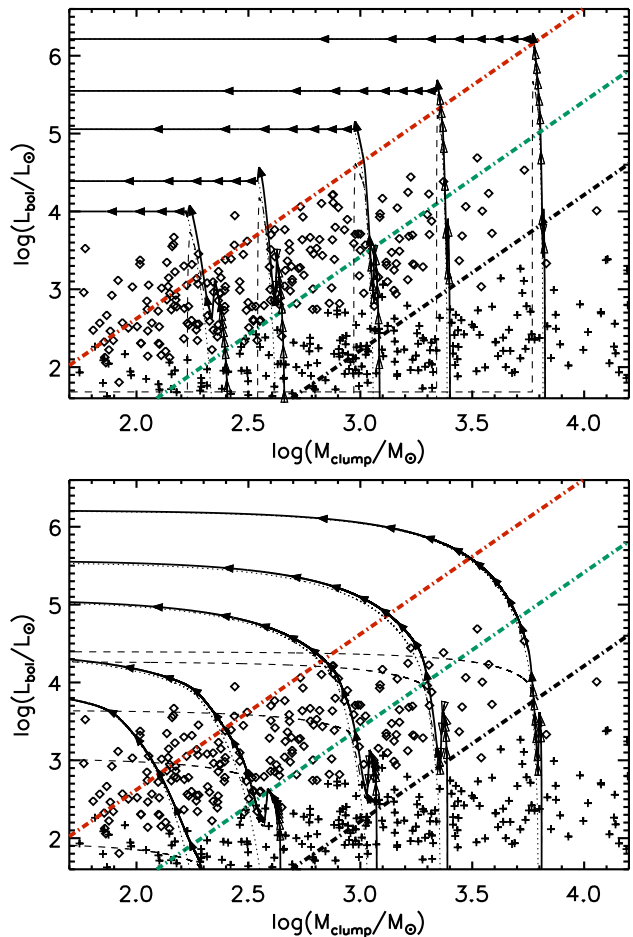


Figure 7. Cold Accretion: L_{bol} - M_{clump} diagrams for the Accelerated Accretion Model and the Constant-Slow Accretion Model with Cold Accretion. The model parameters are as on the corresponding Hot Accretion case provided in Table 1. See the caption of Fig. 6 for further details.

The new interpretation is consistent with the data relating star clusters to the most massive stars as presented by Weidner et al. (2010). Their Fig. 3 shows that there is a minimum mass of the most-massive star for a star cluster of a given size which is approximately three times lower than the average stellar mass. This minimum mass would, of course, be the most likely if drawn randomly from a distribution corresponding to the Initial mass Function. We thus recommend that far-infrared data be interpreted by tracks as shown in Fig. 10.

Fig. 10 also demonstrates that the evolutionary phase of the observed sample of Herschel protostars is more advanced than previously interpreted because the final mass of the stars had been overestimated. The assertion here is that there are far fewer embedded protostars with mass exceeding $30 M_\odot$.

3.4 Radiative Feedback: hot accretion

As the protostar matures, the rapid increase in luminosity leads to a high surface temperature and a high number of extreme ultraviolet photons, N_{Ly} , capable of generating a surrounding source of free-free radio emission as quantified

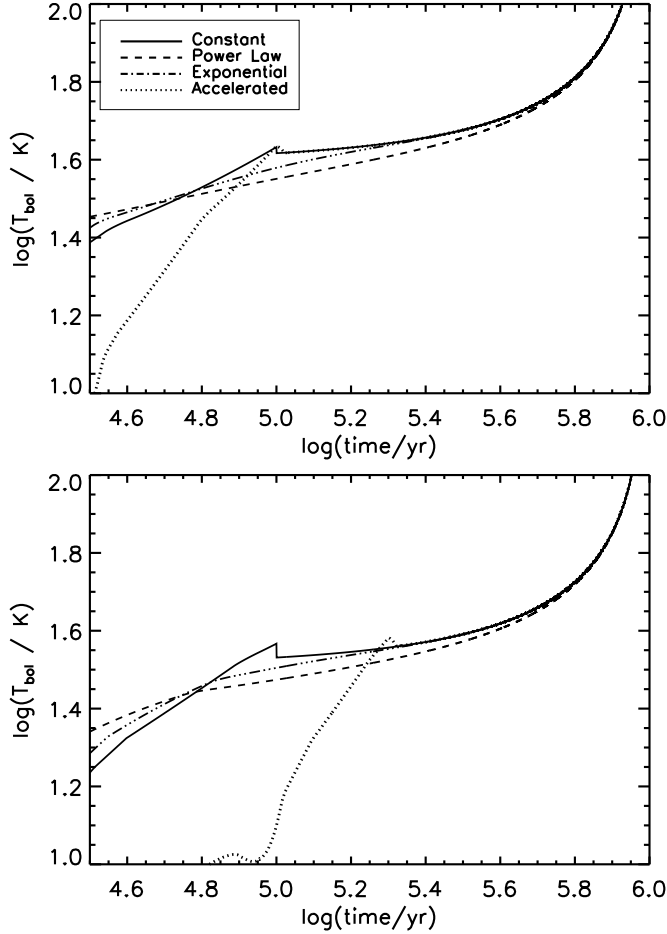


Figure 8. The early evolution of the bolometric temperature for Hot Accretion models which yield $100 M_{\odot}$ (upper panel) and $30 M_{\odot}$ (lower panel) stars, with lines as denoted in Fig. 1 and parameters from Table 1. Hot accretion is assumed here. The panels assume that the initial clump mass is twice that necessary to generate the associated cluster ($A = 0.85$).

in Sub-section 2.4. With this interpretation, we can compare two distinct indicators of evolution: M_{clump}/L_{bol} and N_{Ly}/L_{bol} . Remarkably, both these quantities are, at least in principle, distance independent. It is apparent from Fig. 11 that there is a significant difference between the two extreme models with the Accelerated Accretion tracks for the most massive stars occupying a wider region whereas the Power Law Model predicts much less variation.

We can now suppose that the inner accretion is not spherical but streams onto a limited area of the star, forming accretion hot spots on the surface. Taking a fraction f_{acc} of the accretion to free-fall on to a fraction f_{hot} of the surface area, yields a hot spot temperature T_{hot} given by

$$T_{hot}^4(R, t) = \frac{L_{int} + f_{acc}L_{acc}/f_{hot}}{4\pi\sigma R_*^2}. \quad (35)$$

Contributions to the Lyman flux from the hot spot and the rest of the surface are then added. As shown in Fig.12, the behaviour is different with the the accretion luminosity generating significant early ultraviolet emission. Moreover, the hotspots are very important Lyman emitters for the stars

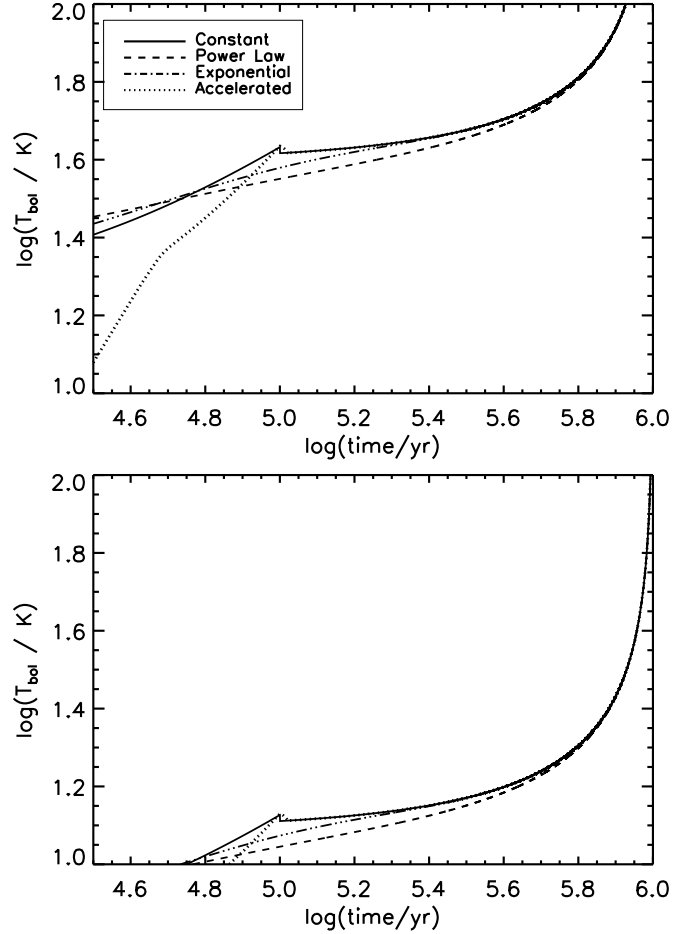


Figure 9. The early evolution of the bolometric temperature for Cold Accretion models with the initial clump mass twice (upper panel) and 9.4 times (lower panel) the fiducial value required to generate the stellar cluster. each model displayed forms a $100 M_{\odot}$ stars, with lines as denoted in Fig. 1 and parameters from Table 1. Although cold accretion is assumed, hot accretion is found to closely follow this behaviour.

of mass $10 - 20 M_{\odot}$ and can dominate the radio emission during the early phases of star formation.

To compare to available data, we plot in Fig. 13 the Lyman photon flux and bolometric luminosity for a typical hot accretion model, with and without hot spots. The observed data are taken from Sánchez-Monge et al. (2013) and are clearly at variance with this model: there remains a significant number of data point lying above the tracks. This problem was discussed by Lumsden et al. (2013), Urquhart et al. (2013) and Sánchez-Monge et al. (2013) on comparing data to the expected Lyman flux from ZAMS stars. Sánchez-Monge et al. (2013) speculated that one resolution could be if there was an extra component from the accretion. The lower panel, however, demonstrates that this is not sufficient in the case where the star itself has formed through spherical accretion: the bloated protostar is too large to permit a significant release of extreme ultraviolet photons through free-fall on to the surface. This conclusion applies to all accretion models discussed here.

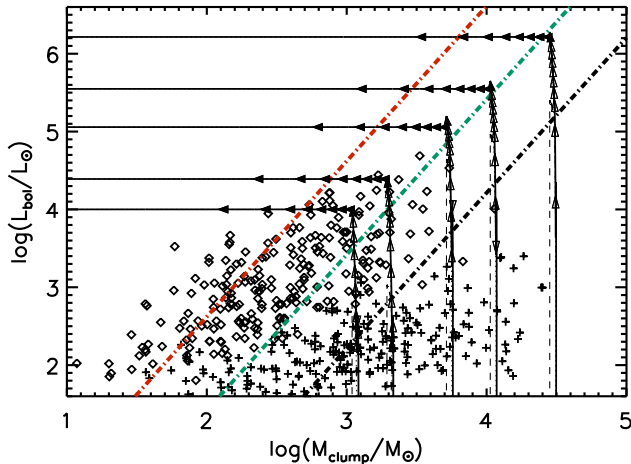


Figure 10. Revised L_{bol} - M_{clump} tracks for the Constant Accretion model with fast cold accretion. The six solid lines correspond to systematically increasing final stellar masses of 8, 10, 15, 30, 50 and $100 M_{\odot}$. The Constant Accretion Model is taken here with final stellar mass, accretion timescale and accretion rates provided in Table 1 but the initial clump has been increased by a factor of 4.7 corresponding to an initial clump mass 9.4 times larger than the final cluster mass. The data are from the Herschel $l = 30^{\circ}$ field as analysed by Veneziani et al. (2013) with protostellar clumps (triangles) and pre-stellar clumps (crosses; taken as bound starless clumps if the temperature is used to derive the relevant internal measure of pressure).

3.5 Radiative Feedback: cold accretion

Cold accretion generates a young star with a considerably smaller radius through the early phases. Hence cold accretion does indeed generate more Lyman photons earlier as shown in the top panel of Fig 14 although not greatly different from the hot accretion examples (note the different axial scales).

We now again suppose that the inner accretion is guided by the magnetic field to form accretion hot spots on the surface. As shown in the lower panel of Fig 14, the behaviour is very different: the accretion luminosity dominates the early UV emission. Moreover, the hotspots are very important Lyman emitters for the stars of mass $10 - 20 M_{\odot}$ and will dominate the radio emission during the early phases of star formation.

Fig. 15 compares the Constant Accretion Model to the ATCA data. While cold accretion does not generate sufficient extreme ultraviolet (top panel) if a considerable fraction of the accreting material is funnelled on to accretion hotspots, then the data can be very well interpreted (lower panel). This implies that the star has formed through a disk rather than spherical infall. However, at some stage, the magnetic field becomes sufficiently strong so that material is diverted and funnelled from the inner disk radius to effectively free-fall on to the surface. The star, of course, has previously formed through the cold accretion and so maintains the relatively small radius. The enhanced Lyman flux is a result of the high accretion on to a small growing protostar. The subsequent temporary extreme fall in the Lyman flux occurs as the bolometric luminosity falls and the star expands.

We find that the conclusion that funnelled accretion

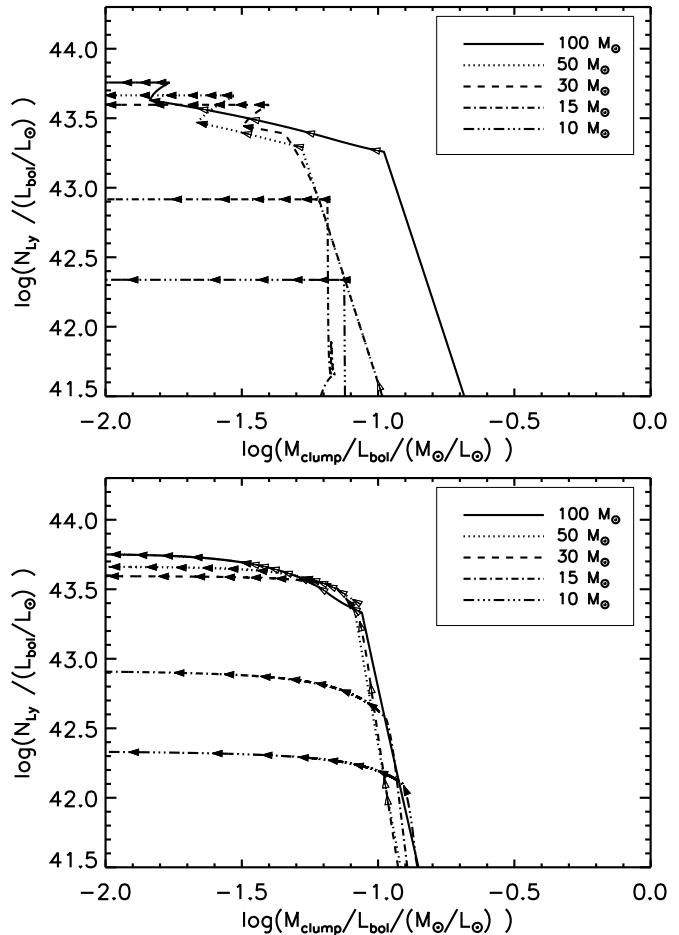


Figure 11. The ratio of Lyman photon flux to bolometric luminosity, N_{Ly}/L_{bol} , against the evolutionary measure M_{clump}/L_{bol} . In this diagram, any large distance ambiguity is excluded. The Accelerating Accretion Model (upper panel) and Power Law Model (lower panel) tracks are displayed for the Hot Accretion model. We also now implicitly assume the 4.7 times higher clump mass deduced in Sub-section 3.3. Here, and in the following figures, the model tracks correspond to stars of final mass 100 (full), 50 (dotted), 30 (dashed), 15 (dot-dashed) and $10 M_{\odot}$ (3-dot-dashed).

onto a compact protostar is occurring is independent of the chosen accretion model, as illustrated in Fig. 16 for two extreme accretion types. Good fits to the ATCA data require hotspot surface areas of less than 3% – 5% for mass fractions of 50% and 75% respectively. These ranges are consistent with the fractions deduced from observations of young stars (Calvet & Gullbring 1998). However, it should be noted that while we concentrate on explaining the enigmatic high Lyman flux, most observed sources are either consistent with ZAMS or are underluminous. Some of these sources are not consistent with that expected on taking into account the additional low-Lyman flux of the associated stellar cluster (Lumsden et al. 2013; Urquhart et al. 2013). In the present context, these sources can be the result of either (1) distributed accretion over the surface and/or (2) single stars in the early-bloating or late Kelvin-Helmholtz contraction phases.

The anomalously high Lyman fluxes only require the

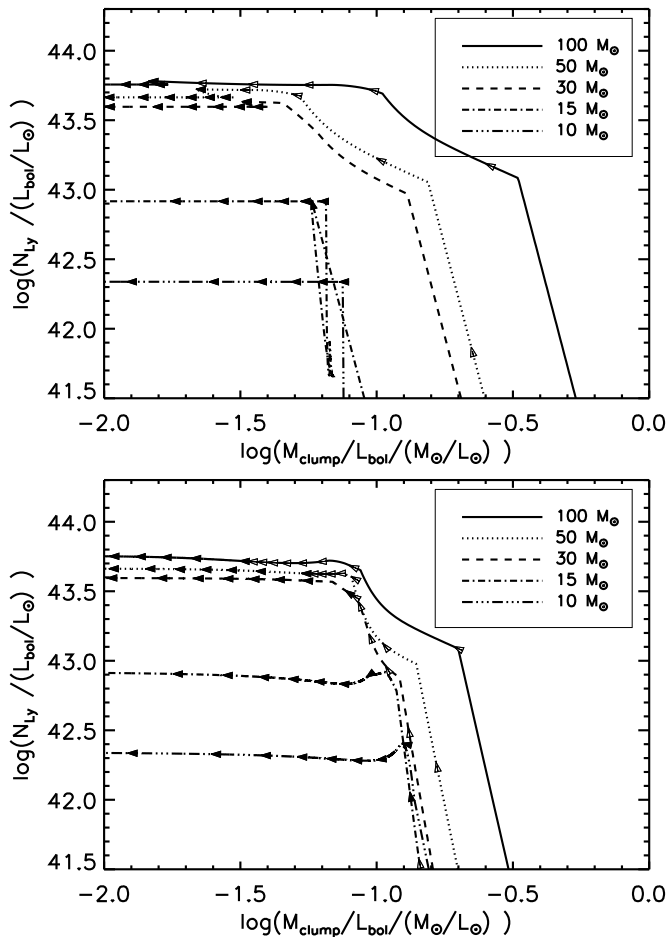


Figure 12. Hot Spot Accretion. The ratio of Lyman photon flux to bolometric luminosity, N_{Ly}/L_{bol} , against the evolutionary measure M_{clump}/L_{bol} . A hot spot covering 5% of the surface upon which 75% of the accretion luminosity is emitted is assumed here. In this diagram, any large distance ambiguity is excluded. The Accelerating Accretion Model (upper panel) and Power Law Model (lower panel) tracks are displayed..

formation of intermediate mass stars. High accretion rates are required to explain some data points. However, as can be seen from Fig. 16, the protostar need only grow up to the beginning of the bloating phase in order to account for the Lyman flux through hot spot accretion.

4 CONCLUSIONS

A model for massive stars has been constructed by piecing together models for the protostellar structure, the inflow from a large clump and the radiation feedback. The framework requires the accretion rate from the clump to be specified. In this first work we consider a specific subset of possible flows. We consider both hot and cold accretion scenarios, identified as the limiting cases for spherical free-fall and disk accretion, respectively. We assume the fiducial cases presented by Hosokawa & Omukai (2009) in the ‘Hot Accretion’ scenario and (Hosokawa et al. 2010) for the ‘Cold Accretion’ structure but it should be noted that there is considerable uncertainty, depending on the assumed initial

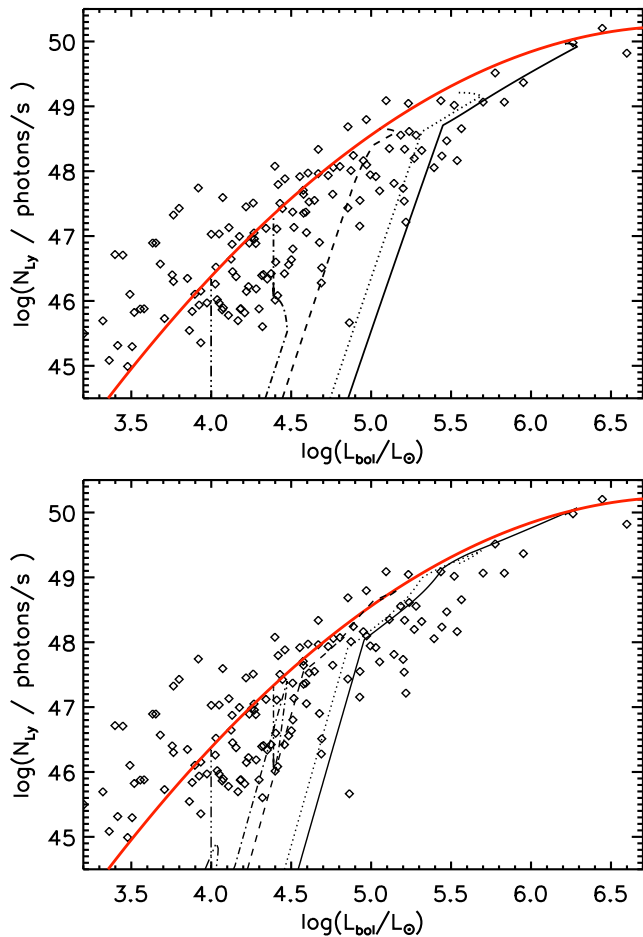


Figure 13. The Lyman photon flux, N_{Ly} , against L_{bol} for the Accelerated Accretion Model with hot accretion. The upper panel displays the tracks with spherical accretion while the lower panel shows the result of channelled accretion on to hot spots covering 5% of the surface upon which 75% of the accretion luminosity is emitted. The data points are taken from Sánchez-Monge et al. (2013), derived from ATCA 18 GHz observations. The thick red line corresponds to the relationship for ZAMS stars, taken from (Panagia 1973). The model tracks correspond to stars of final mass 100 (full), 50 (dotted), 30 (dashed), 15 (dot-dashed) and 10 M_{\odot} (3-dot-dashed).

interior state and the physics of the radiation feedback (see also Kuiper & Yorke (2013)).

Strongly variable accretion rates have been investigated by Smith et al. (2012) as well as Kuiper & Yorke (2013) by utilising hydrodynamic simulations. In both these works, the puffy extended nature of the protostars is evident. Here we only consider smooth evolutions and do not consider accretion outbursts or pulsations, or the jet and outflow properties. We also do not consider binary formation, geometry and inclination effects, or the evolution of the size of the H II region. Hence, this first work sets up the fundamental algorithms and compares results for two recent diagnostic tools.

Models for the formation of massive stars through accretion can be tested by comparing predictions to a range of observational parameters. These include the bolometric and extreme ultraviolet luminosities, the envelope and disk mass,

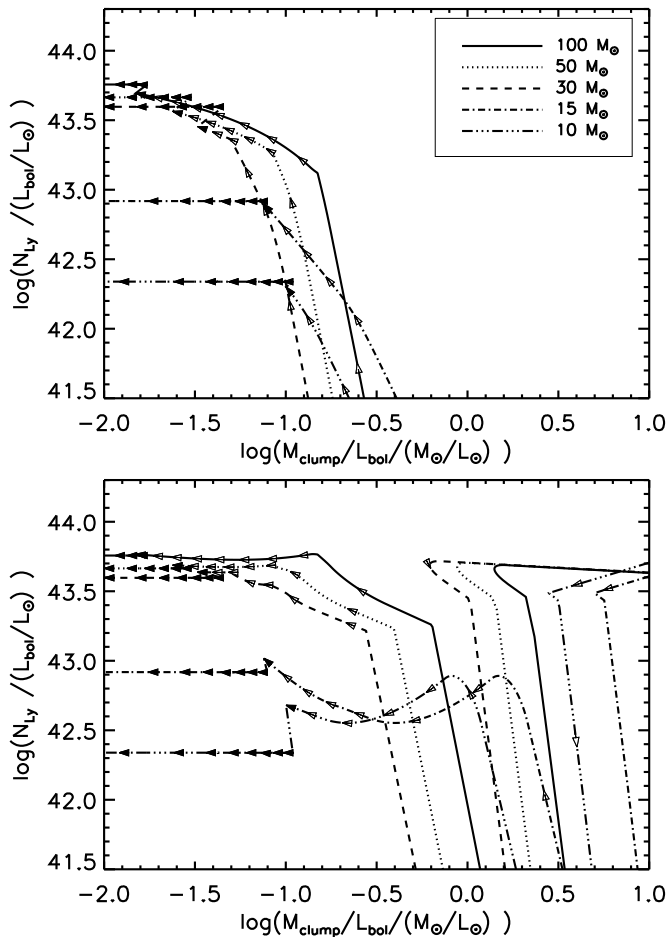


Figure 14. Cold accretion. The ratio of Lyman photon flux to bolometric luminosity, N_{Ly}/L_{bol} , against the evolutionary measure M_{clump}/L_{bol} . In this diagram, any large distance ambiguity is excluded. The Constant Accretion Model with accretion settling on to the star’s surface (upper panel) and with 75% being funnelled on to 5% of the surface at the free-fall speed (lower panel) are displayed.

and the outflow momentum and energy. We here determine possible evolutionary tracks on assuming the variation with time of the accretion rate from a molecular clump on to the star and calculate how the star, envelope and outflow simultaneously evolve. This is achieved by making analytical prescriptions for the components based on current knowledge. We update and extend previous models and confirm previous conclusions that the clump mass must far exceed the accreted mass, most of it being converted into a surrounding cluster of low-mass objects or dispersed.

We find that Accelerated Accretion is not favoured on the basis of the $L_{bol}-M_{clump}$ diagnostic diagram which does not directly provide a test to differentiate the models. Only a slow accretion model can be distinguished in which the star and clump evolve on the same time scale, which is not pursued since it seems unlikely given the contrasting sound-crossing time scales between cores and clumps. This is mainly because the protostar tends to accrete most of its mass within a short time span in all the other models.

Instead, we show that the time spent within each range of bolometric temperature can be closely related to the un-

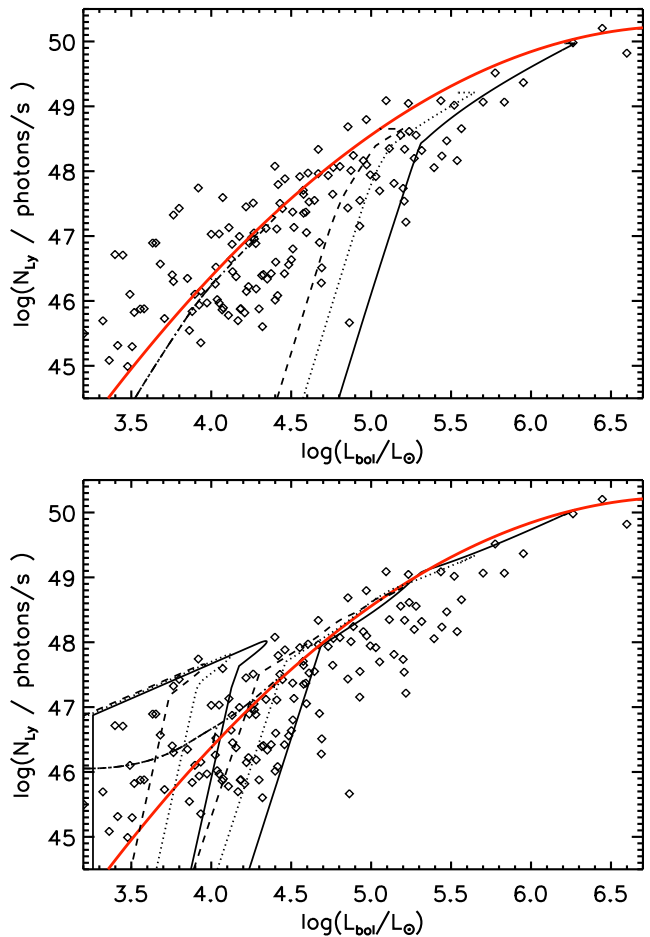


Figure 15. The Lyman photon flux, N_{Ly} , against L_{bol} for the Constant Accretion Model with a compact protostar formed via Cold Accretion. The upper panel displays the tracks with pure disk accretion while the lower panel shows the result of channelled accretion on to hot spots covering 5% of the surface upon which 75% of the accretion luminosity is emitted. The data are taken from Sánchez-Monge et al. (2013), derived from ATCA 18 GHz observations. The thick red line corresponds to the relationship for ZAMS stars, taken from Panagia (1973). The model tracks correspond to stars of final mass 100 (full), 50 (dotted), 30 (dashed), 15 (dot-dashed) and 10 M_{\odot} (3-dot-dashed).

derlying accretion model. As shown in Table 2, Accelerated Accretion generates relatively more sources at low bolometric temperatures. Sets of far-infrared Herschel data covering the temperature range from 20 K – 70 K should provide some insight. However, modelling and observations of the bolometric temperature both remain problematic especially at the low temperatures which can be dominated by unbound non-stellar and pre stellar objects in addition to AGB stars (Veneziani et al. 2013). However, we find a solution which fits the data in which the initial clump mass is four to five times larger than that necessary to generate the associated star cluster corresponding to the mass of the most massive star. We thus generate revised evolutionary tracks which are consistent with statistics for the bolometric temperature. In these revised models, the star remains deeply embedded throughout its formation and the bolometric temperature

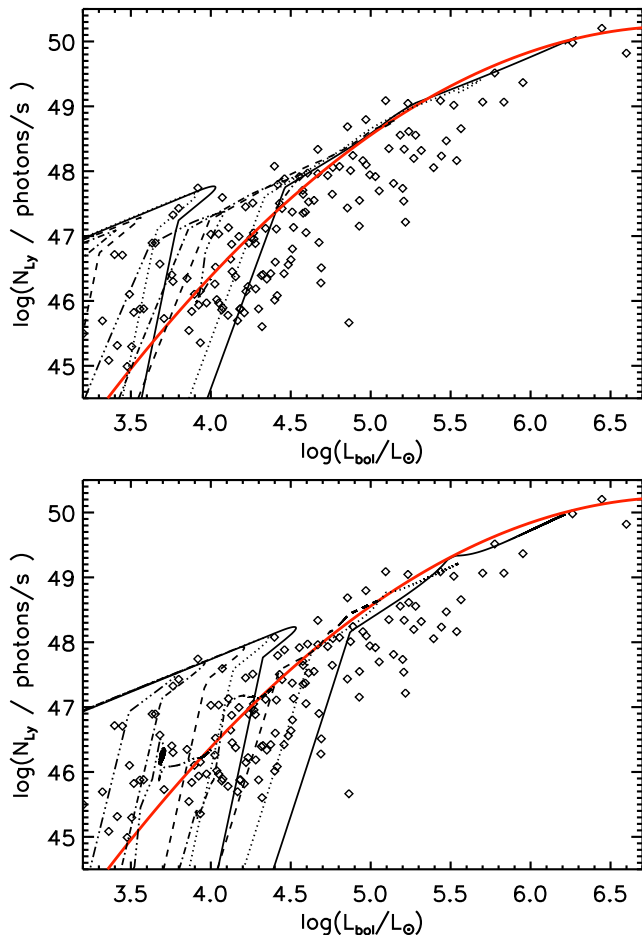


Figure 16. The Lyman photon flux, N_{Ly} , against L_{bol} for the hot spot model combined with the Accelerated Accretion Model (upper panel) and the Power Law Accretion Model (lower panel) with a compact protostar formed via Cold Accretion. The results of channelled accretion on to hot spots covering 5% of the surface upon which 75% of the accretion luminosity is emitted are displayed. The data are taken from Sánchez-Monge et al. (2013), derived from ATCA 18 GHz observations. The thick red line corresponds to the relationship for ZAMS stars, taken from (Panagia 1973). The model tracks correspond to stars of final mass 100 (full), 50 (dotted), 30 (dashed), 15 (dot-dashed) and 10 M_{\odot} (3-dot-dashed).

distribution is no longer a sensitive diagnostic to differentiate between accretion models.

Accretion models may be better tested through a complete sample of hotter protostars with temperatures in the range 50 K to 100 K. In addition, as with their low-mass counterparts, large periodic accretion variations could dominate the statistics.

The Accelerated Accretion Model has been advanced in the literature because we expect the gravitational sphere of influence of a central object to grow as its mass grows. Here, however, with the large accretion rates often assumed, we take an inner envelope to already exist with sufficient mass to meet the later needs of the star and outflow. In this case, the accretion rate depends on how fast mass can flow in from the envelope, through the disk, rather than how massive the central protostar has become.

Finally, we have investigated Lyman fluxes as deduced observationally from radio fluxes. Observationally, it has been shown that objects of luminosity $\sim 10,000 L_{\odot}$ can possess very high Lyman fluxes, inconsistent with their expected stellar temperatures (Sánchez-Monge et al. 2013). We have shown here that the problem is resolvable if the protostar is relatively compact, formed through cold accretion via a disk. However, the present accretion must involve a funnelling free-fall mechanism onto a fraction of the stellar surface estimated to be less than 10%. The mechanism for this remains unknown but if the evidence that massive protostars are configured in the same way as low-mass stars continues to grow, then accretion via magnetic flux tubes and jets driven by magneto-centrifugal processes are conceivable.

The above explanation of the excess Lyman photon flux requires evolution under the Cold Accretion scenario. Hot Accretion falls far short even with the inclusion of hot-spots, as demonstrated in Fig. 13. Cold accretion was defined as accretion on to the photosphere with no back-heating, so that the accreting material has the same entropy as that of the photosphere (Hosokawa et al. 2010). This is a limiting case which may be difficult to realise. It could be generally expected that the rapid mass accretion should be somewhat hot because a fraction of the entropy should be advected into the stellar interior (Hartmann et al. 2011). Taking larger protostellar radii will reduce the Lyman flux; taking radii 50% higher than that predicted for cold accretion, however, does not significantly alter the qualitative of fit to the ATCA data while doubling the radius has a considerable effect. Accurate results will require the implementation of a full stellar evolution code.

The major objective here has been to construct a consistent model which links the components. In the following works, we will investigate the consequences of mass outflows, accretion variations, maser production, thermal radio jets and H II regions with the purpose of determining how their evolutions are coordinated.

5 ACKNOWLEDGEMENTS

I wish to thank Riccardo Cesaroni, Davide Elia, Sergio Molinari and Alvaro Sanchez-Monge for their encouragement and comment.

REFERENCES

- Andre P., Ward-Thompson D., Barsony M., 1993, *ApJ*, 406, 122
- Barentsen G., Vink J. S., Drew J. E., Greimel R., Wright N. J., Drake J. J., Martin E. L., Valdivielso L., Corradi R. L. M., 2011, *MNRAS*, 415, 103
- Behrend R., Maeder A., 2001, *A&A*, 373, 190
- Beltrán M. T., Olmi L., Cesaroni R., Schisano E., Elia D., Molinari S., Di Giorgio A. M., Kirk J. M., Mottram J. C., Pestalozzi M., Testi L., Thompson M. A., 2013, *A&A*, 552, A123
- Beuther H., Henning T., Linz H., Krause O., Nielbock M., Steinacker J., 2010, *A&A*, 518, L78

- Beuther H., Linz H., Tackenberg J., Henning T., Krause O., Ragan S., Nielbock M., Launhardt R., Bihl S., Schmiedeke A., Smith R., Sakai T., 2013, *A&A*, 553, A115
- Beuther H., Schilke P., Sridharan T. K., Menten K. M., Walmsley C. M., Wyrowski F., 2002, *A&A*, 383, 892
- Beuther H., Shepherd D., 2005, in M. S. N. Kumar, M. Tafalla, & P. Caselli ed., *Cores to Clusters: Star Formation with Next Generation Telescopes Precursors of UCHII Regions and the Evolution of Massive Outflows*. pp 105–119
- Blitz L., 1991, in C. J. Lada & N. D. Kylafis ed., *NATO ASIC Proc. 342: The Physics of Star Formation and Early Stellar Evolution Star Forming Giant Molecular Clouds*. p. 3
- Bonnell I. A., Bate M. R., 2002, *MNRAS*, 336, 659
- Bonnell I. A., Bate M. R., 2006, *MNRAS*, 370, 488
- Bonnell I. A., Bate M. R., Clarke C. J., Pringle J. E., 2001, *MNRAS*, 323, 785
- Bontemps S., Andre P., Terebey S., Cabrit S., 1996, *A&A*, 311, 858
- Calvet N., Gullbring E., 1998, *ApJ*, 509, 802
- Calvet N., Hartmann L., Strom S. E., 2000, *Protostars and Planets IV*, p. 377
- Caratti o Garatti A., Froebrich D., Eisloffel J., Giannini T., Nisini B., 2008, *A&A*, 485, 137
- Caratti o Garatti A., Giannini T., Nisini B., Lorenzetti D., 2006, *A&A*, 449, 1077
- Churchwell E., 2002, *ARA&A*, 40, 27
- Curtis E. I., Richer J. S., Swift J. J., Williams J. P., 2010, *MNRAS*, 408, 1516
- Davies B., Hoare M. G., Lumsden S. L., Hosokawa T., Oudmaijer R. D., Urquhart J. S., Mottram J. C., Stead J., 2011, *MNRAS*, 416, 972
- Elia D., Schisano E., Molinari S., et. al 2010, *A&A*, 518, L97
- Faustini F., Molinari S., Testi L., Brand J., 2009, *A&A*, 503, 801
- Foster P. N., Chevalier R. A., 1993, *ApJ*, 416, 303
- Froebrich D., Schmeja S., Smith M. D., Klessen R. S., 2006, *MNRAS*, 368, 435
- Hartmann L., Zhu Z., Calvet N., 2011, *ArXiv e-prints*
- Hosokawa T., Omukai K., 2009, *ApJ*, 691, 823
- Hosokawa T., Yorke H. W., Omukai K., 2010, *ApJ*, 721, 478
- Klaassen P. D., Testi L., Beuther H., 2011, *ArXiv e-prints*
- Kuiper R., Yorke H. W., 2013, *ApJ*, 772, 61
- Larson R. B., 2003, *Reports on Progress in Physics*, 66, 1651
- Lin D. N. C., Pringle J. E., 1987, *MNRAS*, 225, 607
- Lin D. N. C., Pringle J. E., 1990, *ApJ*, 358, 515
- Lumsden S. L., Hoare M. G., Urquhart J. S., Oudmaijer R. D., Davies B., Mottram J. C., Cooper H. D. B., Moore T. J. T., 2013, *ApJS*, 208, 11
- McKee C. F., Ostriker E. C., 2007, *ARA&A*, 45, 565
- McKee C. F., Tan J. C., 2002, *Nature*, 416, 59
- McKee C. F., Tan J. C., 2003, *ApJ*, 585, 850
- Molinari S., Pezzuto S., Cesaroni R., Brand J., Faustini F., Testi L., 2008, *A&A*, 481, 345
- Myers P. C., Adams F. C., Chen H., Schaff E., 1998, *ApJ*, 492, 703
- Natta A., Testi L., Randich S., 2006, *A&A*, 452, 245
- Netterfield C. B., Ade P. A. R., Bock J. J., et. al 2009, *ApJ*, 707, 1824
- Panagia N., 1973, *AJ*, 78, 929
- Peters T., Mac Low M.-M., Banerjee R., Klessen R. S., Dullemond C. P., 2010, *ApJ*, 719, 831
- Planck Collaboration Ade P. A. R., Aghanim N., Arnaud M., Ashdown M., Aumont J., Baccigalupi C., Balbi A., Banday A. J., Barreiro R. B., et al. 2011, *A&A*, 536, A22
- Pringle J. E., 1981, *ARA&A*, 19, 137
- Ragan S., Henning T., Krause O., Pitann J., Beuther H., Linz H., Tackenberg J., Balog Z., Hennemann M., Launhardt R., Lippok N., Nielbock M., Schmiedeke A., Schuller F., Steinacker J., Stutz A., Vasyunina T., 2012, *A&A*, 547, A49
- Ramsay S. K., Varricatt W. P., Davis C. J., Todd S., 2011, *Bulletin de la Societe Royale des Sciences de Liege*, 80, 235
- Rathborne J. M., Jackson J. M., Chambers E. T., Stojimirovic I., Simon R., Shipman R., Frieswijk W., 2010, *ApJ*, 715, 310
- Rathborne J. M., Jackson J. M., Simon R., 2006, *ApJ*, 641, 389
- Reipurth B., Chini R., Krugel E., Kreysa E., Sievers A., 1993, *A&A*, 273, 221
- Rubin R. H., 1968, *ApJ*, 154, 391
- Sánchez-Monge Á., Beltrán M. T., Cesaroni R., Fontani F., Brand J., Molinari S., Testi L., Burton M., 2013, *A&A*, 550, A21
- Saraceno P., Andre P., Ceccarelli C., Griffin M., Molinari S., 1996, *A&A*, 309, 827
- Schmeja S., Klessen R. S., 2004, *A&A*, 419, 405
- Shakura N. I., Sunyaev R. A., 1973, *A&A*, 24, 337
- Shu F., Najita J., Ostriker E., Wilkin F., Ruden S., Lizano S., 1994, *ApJ*, 429, 781
- Shu F. H., 1977, *ApJ*, 214, 488
- Shu F. H., Lizano S., Ruden S. P., Najita J., 1988, *ApJ*, 328, L19
- Simon R., Rathborne J. M., Shah R. Y., Jackson J. M., Chambers E. T., 2006, *ApJ*, 653, 1325
- Smith M. D., 1999, in E. Guenther, B. Stecklum, & S. Klose ed., *Optical and Infrared Spectroscopy of Circumstellar Matter Vol. 188 of Astronomical Society of the Pacific Conference Series, The Evolution of Protostars and their Environments*. p. 117
- Smith M. D., 2000, *Irish Astronomical Journal*, 27, 25
- Smith R. J., Hosokawa T., Omukai K., Glover S. C. O., Klessen R. S., 2012, *MNRAS*, 424, 457
- Spezzi L., de Marchi G., Panagia N., Sicilia-Aguilar A., Ercolano B., 2012, *MNRAS*, 421, 78
- Urquhart J. S., Thompson M. A., Moore T. J. T., Purcell C. R., Hoare M. G., Schuller F., Wyrowski F., Csengeri T., Menten K. M., Lumsden S. L., Kurtz S., Walmsley C. M., Bronfman L., Morgan L. K., Eden D. J., Russeil D., 2013, *MNRAS*
- Varricatt W. P., Davis C. J., Ramsay S., Todd S. P., 2010, *MNRAS*, 404, 661
- Veneziani M., Elia D., Noriega-Crespo A., Paladini R., Carey S., Faimali A., Molinari S., Pestalozzi M., Piacentini F., Schisano E., Tibbs C., 2013, *A&A*, 549, A130
- Weidner C., Kroupa P., Bonnell I. A. D., 2010, *MNRAS*, 401, 275
- Zinnecker H., Yorke H. W., 2007, *ARA&A*, 45, 481